Fabrication of Ultrafine Metal-Oxide-Decorated Carbon Nanofibers for DMMP Sensor Application

Jun Seop Lee,[†] Oh Seok Kwon,[†] Seon Joo Park,[†] Eun Yu Park,[†] Sun Ah You,[†] Hyeonseok Yoon,[‡] and Jyongsik Jang[†,*]

[†]World Class University (WCU) Program of Chemical Convergence for Energy & Environment (C_2E_2), School of Chemical and Biological Engineering, College of Engineering, Seoul National University, 599 Gwanangno, Gwanak-gu, Seoul 151-742, Korea, and [‡]Alan G. MacDiarmid Energy Research Institute, Department of Polymer and Fiber System Engineering, Chonnam National University, Gwangju 500-757, South Korea

ABSTRACT Ultrafine metal-oxide-decorated hybrid carbon nanofibers (CNFs) were fabricated by a single-nozzle co-electrospinning process using a phase-separated mixed polymer composite solution and heat treatment. To decorate metal oxides on the CNF surface, core (PAN) and shell (PVP) structured nanofibers (NFs) were fabricated as starting materials. The core–shell NF structure was prepared by single-nozzle co-electrospinning because of the incompatibility of the two polymers. Ultrafine hybrid CNFs were then formed by decomposing the PVP phase, converting the metal precursors to metal oxide nanonodules, and transforming the PAN to CNFs of *ca.* 40 nm diameter during heat treatment. The decoration morphology of the metal oxide nanonodules could be controlled by precursor concentration in the PVP solution. These ultrafine hybrid CNFs were applied to a dimethyl methylphosphonate (DMMP) chemical sensor at room temperature with excellent sensitivity. The minimum detectable level (MDL) of hybrid CNFs was as low as 0.1 ppb, which is 10–100 times higher than for a chemical sensor based on carbon nanotubes. This is because the metal oxide nanonodules of hybrid CNFs increase the surface area and affinity to DMMP vapor. Our new synthetic methodology promises to be an effective approach to fabricating hybrid CNF/inorganic nanostructures for future sensing technologies.

KEYWORDS: electrospinning · carbon nanofiber · room temperature gas sensing · metal nanoparticle decoration · sensing mechanism

Continuous progress in carbon-based nanomaterials such as carbon nanotubes (CNTs), carbon nanofibers (CNFs), fullerenes, carbon nanohorns, and nanoporous structures has led to the development of devices in the fields of energy and the environment.[1–7] Recently, CNFs and CNTs have received considerable attention because of their remarkable electrical conductivity and good electrochemical stability due to their small dimensions and unique one-dimensional structures.[8,9] Compared with CNTs, CNFs are inexpensive and can be produced with various controlled structures at relatively high rates.[10–12] Therefore, CNFs have been used as materials for hydrogen-storage devices, electrical components, catalytic supports, field-emission devices.[13–17] Transducers in chemical and biosensors made with CNFs are especially high-performing owing to their high conductivity, which can expose either basal graphite planes or edge planes exclusively. Despite these advantages, little research has been done on the development of CNFs as transducers for chemical sensors due to the difficulty of fabricating small-diameter CNFs.

Semiconducting metal oxides (SMOs) with nanostructures have been used for the detection of toxic gases and vapors. Among the various SMOs, TiO_2, ZnO, and SnO_2 are the most well-defined transducers in gas sensor devices.[18–21] ZnO and SnO_2, in particular, show high sensitivity and selectivity to various chemical vapors at high temperatures, including hydrogen, TNT, and chemical warfare agents. However, pristine SMO chemical sensors cannot detect the gases at room temperature. As a result, metal oxides have been used as one component of composite materials for detecting toxic gases and vapors. SMOs have been used with conducting polymers for gas sensor application for use at room temperature.[22–25] The methods for fabricating conducting polymer/SMOs composites are facile owing to functional groups within their structures. However, CNF/SMO and CNT/SMO composites have proven to be difficult to decorate with surface SMOs because of the absence of functional groups. As a result, additional processes are needed to decorate SMOs on surfaces.[26–28] For example, Ramaprabhu *et al.* synthesized SnO_2/CNT heterostructures by combining a thermal CVD method with a chemical solution route.[14] Yang and co-workers fabricated SnO_2/CNF heterostructures by combining electrospinning with subsequent thermal treatment in an Ar/H_2O atmosphere.[29] Zhang *et al.* also reported making SnO_2/CNT heterostructures

* Address correspondence to jsjang@plaza.snu.ac.kr.

Received for review July 4, 2011 and accepted September 11, 2011.

Published online September 12, 2011
10.1021/nn202471f

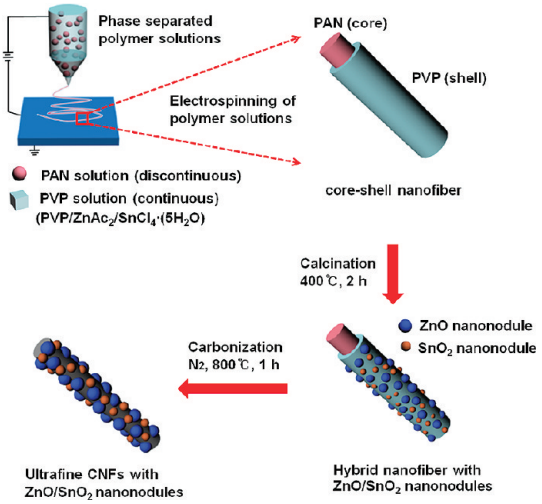

Scheme 1. Illustrative diagram of the sequential fabrication steps for ultrafine hybrid CNFs.

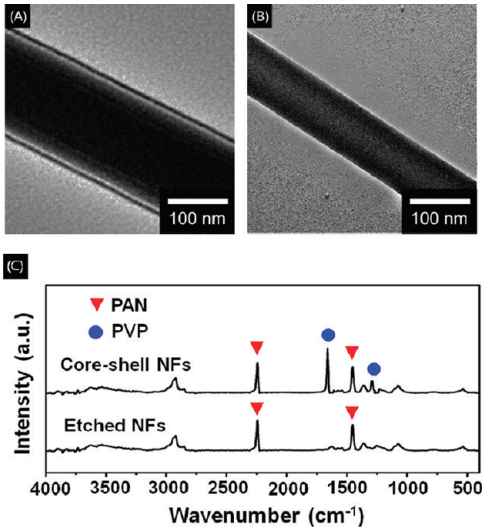

Figure 1. TEM images of (A) electrospun *ca.* 130 nm diameter core (PAN)/shell (PVP) NFs, (B) PVP phase-etched NFs by distilled water in a diameter of *ca.* 90 nm, (C) FTIR of core (PAN)/shell (PVP) NFs and PVP phase-etched NFs.

by a mixed chemical solution route, but this approach needs an additional step to avoid agglomerates.[30]

On the other hand, the single-nozzle co-electrospinning technique that uses phase-separated polymer solutions does not need any additional process to introduce functional groups on the CNF surface in order to decorate them with metal oxides.[12,31,32] Furthermore, this method provides CNFs with smaller diameters than does the conventional electrospinning process.[33−35] Additionally, the co-electrospinning technique is a much simpler and more versatile technique for fabricating CNFs compared with the CVD method.

The threat of odorless and colorless chemical warfare agents such as Sarin, Soman, and Tabun has motivated intensive research on the development of sensitive, selective, and portable gas sensors. These chemical agents are organo-phosphorus compounds that disrupt the mechanism by which nerves transfer messages to organs. Dimethyl methylphosphonate (DMMP), which has a similar structure to Sarin, is a stimulant for the Sarin and also requires a method for its detection in air. Recently, several scientific approaches have been devised to detect these nerve agents, such as colorimetric assay, fluorometric analysis, photoacoustic spectroscopy, enzymatic assay, gas chromatography−mass spectrometry, and molecular imprinting.[36−40] Although all of these methods have advantages, critical limitations still remain to be solved, including low sensitivity, slow response times, operational complexity, high cost, and limited portability.

Here, we present a new bottom-up strategy for fabricating ultrafine hybrid CNFs decorated with metal oxide nanonodules. A single-nozzle co-electrospinning technique is described that can control the nanonodule surface population precisely. The ultrafine hybrid CNFs with metal oxide surface nanonodules were utilized as a transistor for a chemical sensor, and the sensing responses from these sensors were highly sensitive and reversible. The minimum detectable level (MDL) was as low as 0.1 ppb, about 10−100 times higher than that of a chemical sensor based on CNTs.[39,41] This study is the first experimental demonstration of an efficient toxic gas sensor based on ultrafine hybrid CNF/metal oxide nanonodules fabricated by the single-nozzle co-electrospinning fabrication method.

RESULTS AND DISCUSSION

Fabrication of Ultrafine Hybrid CNFs. Scheme 1 illustrates the overall procedure for the fabrication of ultrafine hybrid CNFs based on single-nozzle co-electrospinning. Four components (PAN and PVP/$ZnAc_2$/$SnCl_4 \cdot 5H_2O$) are required to make the initial core−shell nanofiber, which is subsequently calcined and carbonized. The three-component (PVP/$ZnAc_2$/$SnCl_4 \cdot 5H_2O$) PVP solution and the PAN solutions are separated as continuous (surrounding) and discontinuous (droplet) phases due to the incompatibility of the two polymers in the mixture solution as a result of their intrinsic physical properties, in particular, their viscosities. The low-viscosity polymer would be the continuous phase, whereas the high-viscosity one would form the discontinuous phase in the mixture solution.[31] PAN and PVP solution viscosities were measured; that of PAN (0.081 Pa·S) was nearly 6 times higher than that of PVP (0.013 Pa·S). Thus, in the mixed solution, the PVP solution was the continuous phase and the PAN solution was the discontinuous phase (Supporting Information, Figure S1).

The PAN/PVP mixture was electrospun onto the collector under a continuous voltage and formed 130 nm diameter core (PAN)/shell (PVP) NFs (Figure 1A). During electrospinning, the inner discontinuous phase receives

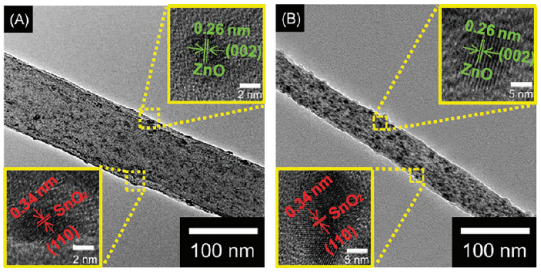

Figure 2. TEM images of (A) calcined hybrid NFs containing ZnO and SnO_2 nanocrystalline nuclei on the shell surface (PVP) with a diameter of *ca.* 90 nm; HRTEM images are shown in the inset (green, ZnO; red, SnO_2; the diameters of ZnO and SnO_2 are 4 and 3 nm, respectively), and (B) carbonized ultrafine hybrid CNFs contained ZnO and SnO_2 nanonodules on the surface with a diameter of *ca.* 40 nm; HRTEM images are displayed in the inset (green, ZnO; red, SnO_2; the diameters of ZnO and SnO_2 are 12 and 8 nm, respectively).

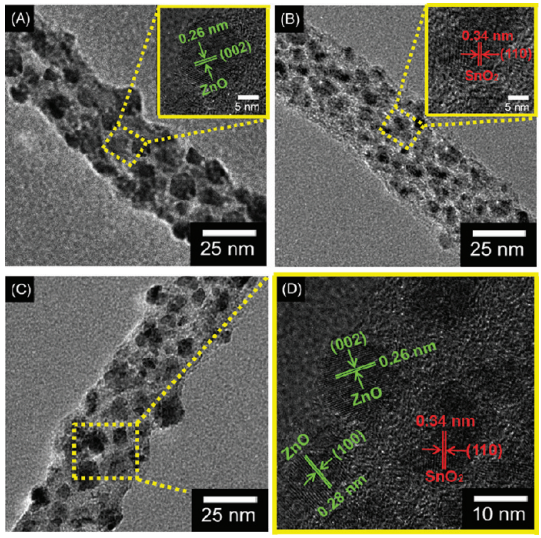

Figure 3. TEM and HRTEM (inset) images of types of metal oxides on the CNF surfaces (A) CNF1 (with ZnO nanonodules (green)) and (B) CNF2 (with SnO_2 nanonodules (red)). (C) TEM image of CNF3 (with ZnO and SnO_2 nanonodules) and (D) HRTEM image of CNF3 nanonodules (green, ZnO; red, SnO_2).

only the force applied to its surface from the outer continuous phase, that is, from the action of the electric forces acting on the outer surface, as it is drawn into the jet. Therefore, the continuous outer layer undergoes ordinary single-nozzle electrospinning from the Taylor cone tip, with the occasional droplet of the discontinuous phase becoming trapped at the cone base.[21] TEM and FTIR analyses of distilled-water-etched NFs confirmed the core–shell structure. TEM of NFs where etching had removed the PVP shell showed the remaining core phase NFs to be 90 nm in diameter (Figure 1B). FTIR of the core–shell NFs displayed absorption bands for PAN (2245 and 1466 cm^{-1}) and PVP (1661 and 1285 cm^{-1}), but the etched NFs showed only the PAN peaks (2245 and 1466 cm^{-1}) (Figure 1C).

The ZnO and SnO_2 precursors were dispersed as Zn^{2+} and Sn^{4+} ions in the PVP (shell) phase of electrospun core–shell nanofibers. The Zn^{2+} and Sn^{4+} were dispersed in the PVP phase with a coordinate covalent bond with partial negative charge of O atom in the PVP structure (see Supporting Information Figure S2). Electrospun core–shell NFs were calcined at a rate of 2 °C/min and maintained for 2 h at 400 °C. During this process, the Zn^{2+} and Sn^{4+} were converted to ZnO and SnO_2 nanocrystalline nuclei on the surface of the PVP layer (Figure 2A). The diameters of the calcined hybrid nanofiber was *ca.* 90 nm, and the ZnO and SnO_2 surface nuclei were 4 and 3 nm, respectively (inset Figure 2A). A calcination temperature of 400 °C was chosen to prevent decomposition of the PAN/PVP polymer yet enable generation of the metal oxide nanocrystalline nuclei. The calcined hybrid NFs were then carbonized at a rate of 5 °C/min and maintained for 1 h at 800 °C under N_2 flow to form ZnO/SnO_2 nanostructured nodules on the CNF surface, that is, ultrafine hybrid CNFs with a diameter of *ca.* 40 nm (Figure 2B). The size of ZnO and SnO_2 nanonodules were 12 and 8 nm, respectively (inset Figure 2B). Furthermore, Raman spectra of calcined hybrid NFs and carbonized hybrid CNFs confirmed that graphitic carbon nanofibers were made by carbonization hybrid NFs (see Supporting Information Figure S3).

Characterization of Ultrafine Hybrid CNFs. The degrees of crystallinity of the ZnO and SnO_2 nanonodules on the hybrid CNF surface were confirmed by TEM, HRTEM, XRD, and XPS. The TEM images in Figure 3A,B clearly show hybrid CNFs with metal nanonodules on the surface (the CNFs with ZnO nanonodules and SnO_2 nanonodules are indicated as CNF1 and CNF2, respectively). The ZnO nanonodules displayed an interplanar spacing of 0.26 nm for the (002) plane, corresponding to a hexagonal wurtzite lattice (see the inset of Figure 3A). The SnO_2 nanonodules showed an interplanar spacing of 0.34 nm for the (110) plane of the rutile lattice (see the inset of Figure 3B). Moreover, the TEM of hybrid CNFs with ZnO/SnO_2 nanonodules (CNF3) displayed dispersed ZnO (black spots) and SnO_2 (gray spots) nanonodules (Figure 3C). The crystallite size of the ZnO (*ca.* 12 nm) was larger than that of SnO_2 (*ca.* 8 nm), while the population of SnO_2 nanonodules was higher than that of ZnO ones. This was attributed to different sintering behaviors: ZnO sinters more easily and consequently tends to form larger nanonodules.[42] HRTEM (Figure 3D) shows the coexistence of nanonodules with the (002) and (100) planes of a hexagonal wurtzite lattice for the ZnO nanonodules and the (110) plane of a rutile lattice for the SnO_2 nanonodules.

Figure 4 shows XRD patterns for the metal oxide nanonodules on the CNF surface. The ZnO nanonodules for CNF1 had six reflection peaks, and all could be indexed as the hexagonal wurtzite structure (JCPDS 36-1451). The (110) layer was evident in the HRTEM

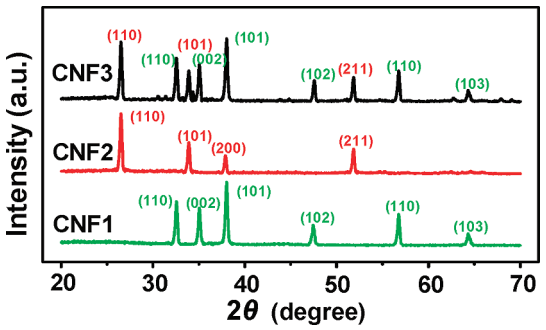

Figure 4. XRD patterns for the metal oxide nanonodules on the CNF surface that are CNF1 (with ZnO (green)), CNF2 (with SnO_2 (red)), and CNF3 (with ZnO/SnO_2 (black)).

analyses. The SnO_2 nanonodules in CNF2 produced four reflection peaks attributable to the rutile structure (JCPDS 41-1445). The (110) layer was evident in the HRTEM analyses. All reflection peaks of the XRD pattern for the ZnO/SnO_2 hybrid nanonodules matched those for the hexagonal wurtzite ZnO and tetragonal rutile SnO_2 structures. Furthermore, no peaks for potential impurities such as SnO, $ZnSnO_3$, and Zn_2SnO_4 were observed. These results verify that the pure nanonodules had high crystallinity following the heat treatment.

The chemical composition of hybrid CNFs was compared with pristine CNFs by X-ray photoelectron spectroscopy (XPS). Figure 5A shows the complete spectra over the range of 0−1200 eV. These overview spectra demonstrate that C, Sn, Zn, O, and N atoms were present in the CNF3, whereas pristine CNFs had only C, O, and N elements present. The N 1s peak was attributed to N-containing gaseous contaminants. The high-resolution XPS spectra for the C 1s region around 285 eV are shown in Figure 5B. It has been deconvoluted into three components. The peak at 284.6 eV is attributed to C−C bonds and is believed to have originated from an amorphous carbon phase or from adventitious carbon. The peak at 285.6 eV is characteristic of C−O groups. The small broad band at 290−291 eV can be assigned to the shakeup $\pi-\pi^*$ satellite, which is a common feature of graphitic carbon in XPS spectra. The C 1s peaks for the CNF3 were not shifted relative to those for pristine CNFs, confirming that the structure of the CNFs remained unchanged after the formation of the SnO_2 and ZnO nanonodules. Figure 5C shows the high-resolution XPS spectra for the Sn 3d peak. The spin−orbit components ($3d_{3/2}$ and $3d_{5/2}$) are observed at 495.8 and 487.3 eV. The splitting of the 3d doublet was 8.5 eV, indicating that the valence state of the Sn was +4. Figure 5D presents the high-resolution XPS spectra for the Zn 2p peak. The spin−orbit components ($2p_{3/2}$ and $2p_{1/2}$) are observed at approximately 1022.5 and 1045.5 eV, indicating that the valence state of the Zn was +2. Thus, it can be concluded that the ZnO/SnO_2 nanonodules were composed of Zn(II), Sn(IV), and O, in agreement with the XRD results.

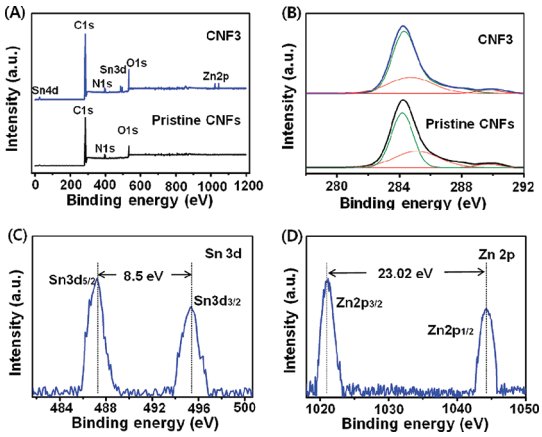

Figure 5. XPS patterns of (A) fully scanned spectra of CNF3 (blue) and pristine CNFs (black) and high resolution of (B) C1s for the CNF3 (blue) and pristine CNFs (black), (C) Sn 3d, and (D) Zn 2p for the CNF3.

The population of metal oxides on CNF3 was controlled using various precursor concentrations (0.5 to 2.0 wt %) (Figure 6). As shown in the inset FE-SEM images, the diameter of CNF3 was *ca.* 40 nm. The PVP polymer solution used to fabricate CNF3 has two critical functions. First, it increases the spinability of the PAN polymer solution because the PVP solution is less viscous than the PAN solution, and so addition of PVP solution reduces the viscosity of mixed polymer solutions. As a result, the diameter of the electrospun NFs was reduced from 220 to 130 nm by adding the PVP solution (Supporting Information, Figure S4). Furthermore, PAN is easily transformed into carbon (*ca.* 40−50%) during carbonization, whereas PVP is decomposed without carbon residue. As a result, the diameter of CNFs from PAN/PVP NFs is more diminished during thermal treatment than are PAN NFs. The diameters of hybrid CNFs from PAN and PAN/PVP were 130 and 40 nm, respectively (Supporting Information, Figure S5). Second, the PVP behaves as a site for nanocrystalline nucleation on the CNF surfaces during thermal decomposition. The PVP, which holds the metal precursors, is the shell phase of PAN/PVP NFs. Precursors added to the PVP solution will lead to metal oxides decorating the CNF surfaces following carbonization. Moreover, by controlling the amount of precursor added to the PVP solution, it is possible to control the population of metal oxides. At low concentrations, the ZnO/SnO_2 population is not sufficient to completely cover the surface, and the particle size is very small (Figure 6A). On the other hand, at high concentrations, the population is too high to grow nanonodules, and a metal oxide layer forms instead (Figure 6F). The decoration amount of metal oxides was quantified by TGA estimate (see Supporting Information, Figure S6).

Real-Time Responses of the Sensor Based on CNFs to DMMP Gas. The randomly stacked arrangement of CNFs prepared by the drop-casting method had a contact resistance higher than the uniform array obtained by

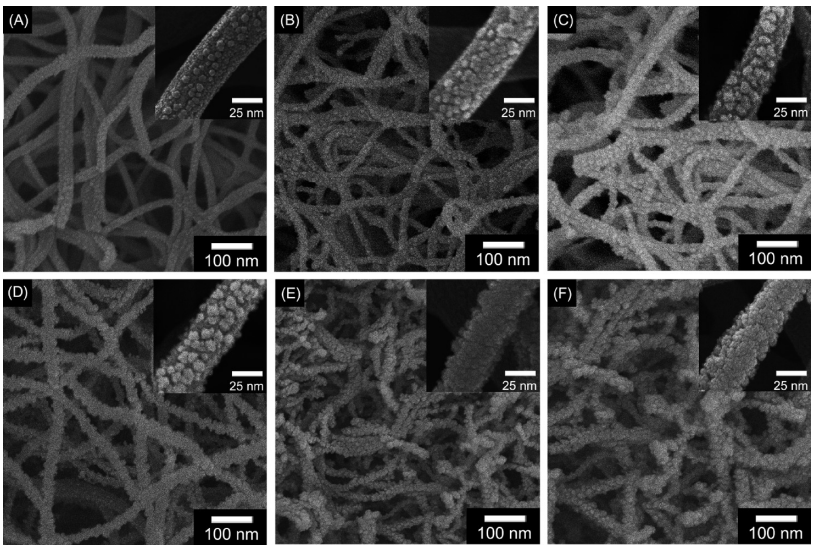

Figure 6. Low- and high-resolution (inset) FE-SEM images of CNF3 that is composed various concentration of $ZnAc_2$, and $SnCl_4 \cdot 5H_2O$ in the PVP solution (A) 0.5 wt %, (B) 0.75 wt %, (C) 1 wt %, (D) 1.25 wt %, (E) 1.5 wt %, and (F) 2 wt % with a diameter of 40 nm.

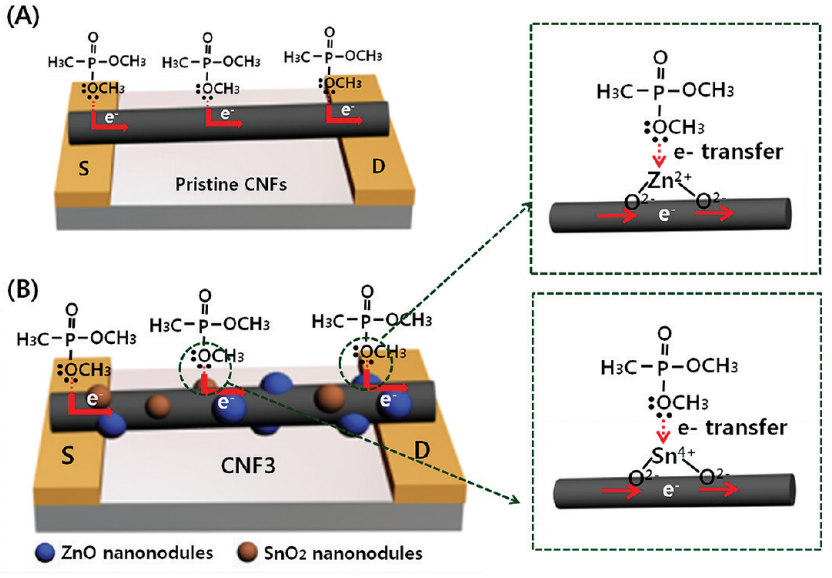

Figure 7. DMMP vapor detecting mechanism of (A) pristine CNFs and (B) CNF3.

spin-coating owing to interruption of the conductive pathway through the accumulated fiber−fiber assembly (see Supporting Information Figure S7). Therefore, to determine the sensing performance of a chemical sensor based on using uniformly dispersed CNFs as the signal transducer, CNFs were deposited on the electrode by spin-coating and their electrical responses were monitored in real time.[43]

The uniformly dispersed CNFs on the sensor substrate rapidly detected DMMP gas at room temperature *via* charge transfer. CNF surfaces adsorb DMMP vapor and provide a continuous pathway for charge carriers (Figure 7A). DMMP is a strong electron donor, so when CNFs are exposed to DMMP vapors, electrons are transferred from DMMP to the CNFs.[41,44] This leads to a decrease in the number of holes in the CNFs, thereby increasing electrical resistance. The interaction of ZnO/SnO_2 nanonodules with DMMP vapor may further enhance sensitivity (Figure 7B). This reaction is induced through chemical adsorption between a methoxy O atom of DMMP and the Zn/Sn atoms. This corresponds to the interaction of a lone electron pair of the O atom and a vacant orbital of an acidic surface site, such as Zn^{2+} or Sn^{4+} cations.[21,45] Chemical adsorption between the O atom of DMMP and the Zn/Sn atoms conducts electrons from DMMP to holes in the CNFs, resulting in increased sensitivity to DMMP gas.

The amounts and types of metal oxides on the CNF surfaces affect the sensing performance of the DMMP gas sensor. The real-time responses of hybrid CNFs

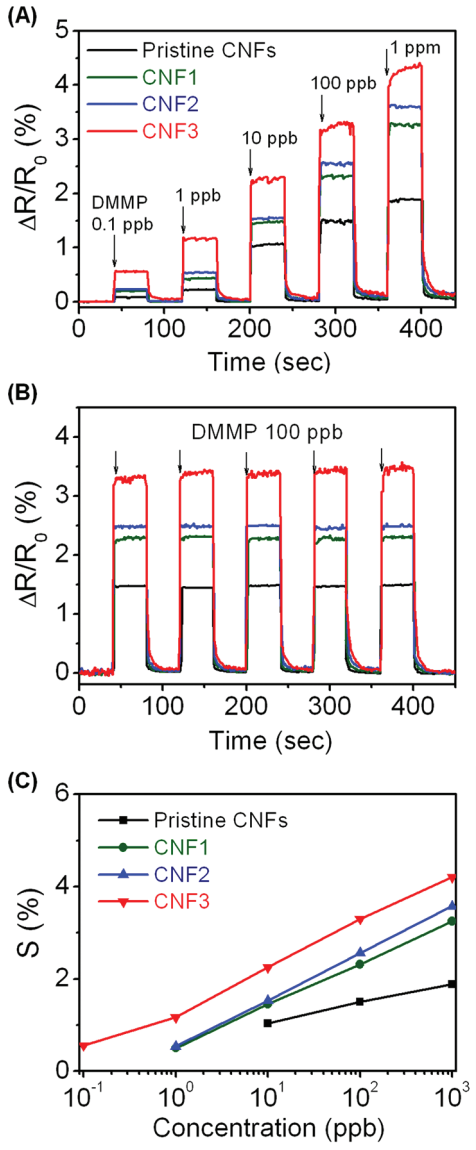

Figure 8. Reversible and reproducible responses are measures at a constant current value (10^{-6} A) with amount and type of metal oxides on the CNF surfaces (black, pristine CNFs; green, CNF1 with 1 wt % ZnO; blue, CNF2 with 1 wt % SnO_2; and red, CNF3 with 1 wt % ZnO and SnO_2). Normalized resistance changes upon (A) sequential exposure to various DMMP vapor concentration, (B) periodic exposure to DMMP vapor of 100 ppb (R_0 values of 3×10^3 Ω), (C) calibration line of hybrid CNFs as a function of DMMP vapor concentration (R_0 values of 3×10^3 Ω).

were measured for various concentrations of DMMP (Figure 8). When hybrid CNF sensors were exposed to DMMP gas at room temperature, excellent sensitivities and rapid response/recovery times were observed. These gas sensors displayed reversible and reproducible real-time responses. Figure 8A shows the responses upon sequential exposure as a function of analyte concentration (0.1, 1, 10, 100, and 1000 ppb). Response times were less than 1 s for all gas concentrations, and the recovery time was approximately 30 s for CNF3 (0.1 ppb of DMMP). Response and recovery times were respectively defined as the times required for the sensor signal to reach 90% of the saturation and original values. Moreover, the sensitivities and recovery times of the hybrid CNF sensors increased with increasing Brunauer–Emmett–Teller (BET) surface areas (BET (m^2/g): CNF3 (258) > CNF2 (215) > CNF1 (210) > pristine CNFs (170)). The minimum detectable level (MDL) also increased in the same order. A higher BET surface area provides more enhanced interaction with analytes, and the recovery time is slower due to desorption of DMMP molecules from the hybrid CNF backbones.

Figure 8B presents the electrical response of CNFs upon periodic exposure to 100 ppb of DMMP. The cyclic tests revealed similar responses and excellent sensing properties over 10 cycles. The hybrid CNF gas sensors were reversible for detecting DMMP gas. Figure 8C plots the sensitivity change of the sensors as a function of vapor concentration. At low concentrations (<0.1 ppb), the hybrid CNF sensors displayed nonlinear changes in sensitivity; the normalized resistance change (S) should be zero at 0 ppb. Linear behavior was observed over a wide range of concentrations of 0.1–1000 ppb for CNF3, 1–1000 ppb for CNF1 and CNF2, and 10–1000 ppb for pristine CNFs. Thus, the hybrid CNF gas sensors demonstrated reversible and reproducible responses for different analyte vapor concentrations, and their responses were more pronounced with increasing analyte vapor concentration.

DMMP gas sensitivity was also affected by the concentration of metal oxide nanonodules on the CNF3 surface (Figure 9). Reversible and reproducible real-time responses were displayed upon sequential exposure to DMMP as a function of analyte concentration. CNF3 with 1 wt % metal oxide had higher sensitivity than CNF3 with 0.5 or 1.5 wt % because 1 wt % concentration provides a higher BET surface area ((m^2/g): 1 wt % (258) > 0.5 wt % (200) > 1.5 wt % (173)) and carbon surface sensing effect, that is, electron transfer from DMMP to carbon holes. Furthermore, the sensitivity of the 1.5 wt % case was lower than that of the 0.5 wt % case because of the formation of metal oxide aggregates rather than nanonodules. Increasing the decoration level of metal oxides led to higher sensitivity than pristine CNFs until 1 wt % concentration. Above this level, the sensitivity decreased with increasing amounts of dispersed nanonodules. As a result, surface metal oxide concentrations greater than 1 wt % reduced the affinity to DMMP gas. The responses to 100 ppb of DMMP vapor for various ZnO/SnO_2 concentrations (0 to 2 wt %) are shown in Figure S8 (Supporting Information). The optimal weight of nanonodules was *ca.* 1 wt %. Table S1 (Supporting Information) shows the sensing performance of the CNF3 sensors with various metal oxide concentrations.

The electrical responses of the CNF sensors upon periodic exposure to DMMP at 100 ppb are presented in Figure 9B. Cyclic testing demonstrated

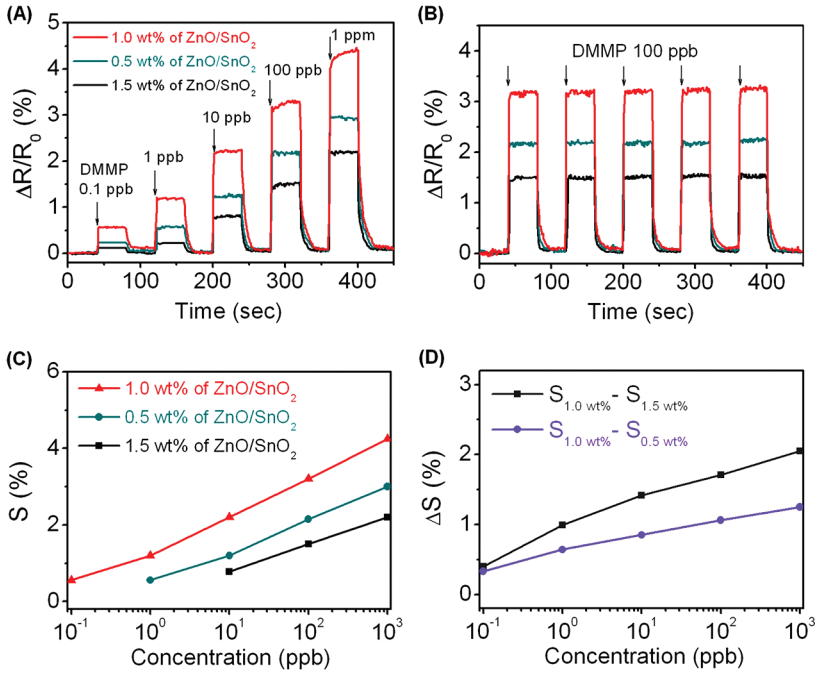

Figure 9. Reversible and reproducible responses are measured at a constant current value (10^{-6} A) with metal oxide concentration. The diverse inorganic concentration of CNF3 is made from various wt % of $ZnAc_2$ and $SnCl_4 \cdot 5H_2O$ (black, 1.5; green, 0.5; red, 1 wt %). Normalized resistance changes upon (A) sequential exposure to various DMMP vapor concentration, (B) periodic exposure to DMMP vapor of 100 ppb (R_0 values of 3×10^3 Ω), (C) calibration line of CNF3 as a function of DMMP vapor concentration (R_0 values of 3×10^3 Ω), (D) differential responses (ΔS) to DMMP vapor concentration for the cases of 1 wt %/0.5 wt % (purple) and 1 wt %/1.5 wt % (gray) metal oxide concentration.

similar responses and excellent sensing properties over 10 cycles. Figure 9C shows the sensitivity change (S) of hybrid CNFs to the amount of dispersed oxides as a function of DMMP vapor concentration. At low concentrations (<0.1 ppb), the sensors displayed a nonlinear change in sensitivity. On the other hand, linear behavior was observed over a wide concentration range of 0.1−1000 ppb for 1 wt % CNF3. The MDLs were 0.1, 1, and 10 ppb for 1.0, 0.5, and 1.5 wt % ZnO/SnO_2 cases, respectively, corresponding to decreasing BET surface area and carbon surface detecting effects. Figure 9D plots the differential response to DMMP vapor concentration for the cases of 1 wt %/0.5 wt % and 1 wt %/1.5 wt % metal oxide concentrations. The differential response was linear over the DMMP concentration range of 0.1 to 1000 ppb.

CONCLUSION

Ultrafine, 40 nm diameter CNFs decorated with metal oxide nanonodules on the fiber surfaces can be fabricated by phase-separated polymer solution co-electrospinning followed by thermal treatment. To our knowledge, this is the first demonstration of the manufacture of hybrid metal oxide composite CNFs using the single-nozzle co-electrospinning method. In this process, PVP provides two critical contributions. First, adding a PVP solution enhances spinability by reducing the viscosity of the polymer composite solution and thereby decreases the diameter of the electrospun NFs. PVP is decomposed during carbonization of the CNF3. Second, the PVP solution containing Zn/Sn precursors forms the shell of NFs so that, during heat treatment, ZnO/SnO_2 nanoodules are formed and sintered concurrently with decomposition of the PVP. We systemically investigated the sensitivity of hybrid CNFs to DMMP vapor by varying the types and amounts of metal oxides dispersed on the fiber surfaces. A hybrid CNF sensor revealed sensitivity values in the order CNF3 > CNF2 > CNF1 > pristine CNFs. These sensing values correlated with increasing BET surface area and interaction of the DMMP gas with the metal oxide nanonodules. CNF3 detected 0.1 ppb DMMP vapor at room temparature. The response time of hybrid CNFs was less than 1 s, and the recovery time decreased gradually with increasing number of oxide components. Additionally, the concentration of metal oxides critically affected the sensitivity to DMMP vapor. The sensitivity increased with dispersed ZnO/SnO_2 concentration up to 1 wt % but then decreased above this concentration. Decreasing carbon surface sensing and adsorption site areas diminished sensitivity to DMMP. Co-electrospinning of phase-separated polymer solutions by single-nozzle co-electrospinning is a facile approach to fabricating ultrafine CNFs decorated with metal oxides that have excellent sensitivity to DMMP vapor at room

temperature. This study provides an effective way to control the surface concentration of metal oxides. A logical extension of this research would be to explore fabrication of dual metal oxide fibers.

MATERIALS AND METHODS

Materials. Poly(acrylonitrile) (PAN, M_w = 150 000), poly(vinylpyrrolidone) (PVP, M_w = 1 300 000), zinc acetate ($ZnAc_2$), and tin(IV) chloride pentahydrate ($SnCl_4 \cdot 5H_2O$) were purchased from Aldrich Chemical Co. *N*,*N*-Dimethylformamide (DMF, Aldrich) was used as a chemical solvent of PAN and PVP solution.

Fabrication of Ultrafine Hybrid CNFs. PAN solution was prepared by dissolving 1.0 g of PAN in 10 mL of DMF at 80−90 °C for 1 h with vigorous stirring. PVP solution was prepared by dissolving 1 g of PVP and various amount of mixture $Zn(Ac)_2/SnCl_4 \cdot 5H_2O$ solution in 10 mL of DMF at 50 °C for 2 h with vigorous stirring. Then, PAN and PVP solutions were mixed at 80−90 °C for 3 h. The viscous hybrid solution obtained was injected from a syringe. The diameter of the needle in the electrospinning was 0.1 mm, and the needle was connected to the positive terminal of a power supply. The voltage was conducted at 15 kV, and the solution was delivered to the syringe by a syringe pump (KD Scientific, USA). The flow rate of the syringe pump was fixed at 5 μL/min, and the distance between the nozzle and collector was 15 cm. The electrospun core−shell NFs should perform calcinations at proper temperature to construct a metal oxide crystal before the carbonization process. Typically, the core−shell NFs performed calcination at 400 °C for 2 h at a heating rate of 1 °C/min. Then the calcined NFs were carbonized at 800 °C for 1 h in nitrogen gas flow at a heating rate of 5 °C/min.

Deposition of Hybrid CNFs on the Interdigitated Electrode Array (IDA). The hybrid CNFs (0.5 wt % in ethanol soluion) were prepared by ultrasonication to deposition on the as-prepared IDA. The ultrasonication was carried out using an ultrasonic homogenizer (Autotune 750 W, Cole-Parmer Instruments, Vernon Hills, Illinois, USA). The ultrasonication equipment was operated at a frequency of 20 kHz by using a titanium probe with a tip diameter of 12 mm. The ultrasonication was carried out with an ultrasonic intensity of 15 W cm^{-2} for 40 min. The samples were introduced by a drop-casting method on top of the IDA in order to reduce the contact resistance between internanofibers. The physical adsorption of CNFs on the substrate was followed by drying at 25 °C in an inert atmosphere for 1 h to obtain good electrical ohmic contact between the CNFs and electrodes. In the droplet process, a spin-coating method (1000 rpm, 45 s) was used for introducing the uniformly controlled array, while a randomly disordered sensor substrate through a drop-casting method was employed as the control experiment.

Structure and Preparation of the Sensor Device. The hybrid CNF gas sensors were mounted inside a one-side opened cell having an approximate volume of 10 cm^3. Four mass flow controllers (MFCs) were connected to form a single output that supplied gas to the cell. In this work, two lines of MFCs were employed: one for synthetic air and one for a low concentration. One line of MFCs was connected to the other line of MFCs through the bubbler to vaporize the DMMP solution. The concentrations of the gases were varied by changing the synthetic air to analyte gas ratio while maintaining a constant flow rate of 2000 sccm. The sensor was exposed to a sequence of VOCs pulses for a fixed period, and the cell was purged with synthetic air between each pulse to enable recovery of the sensor.

Characterization of Hybrid CNFs. Photographs of transmission electron microscopy (TEM) and high-resolution transmission electron microscopy (HRTEM) were obtained with a JEOL JEM-200CX and JEOL JEM-3010, respectively. In the sample preparation, nanomaterials diluted in ethanol/methanol were cast onto a copper grid. A JEOL 6700 was used to obtain field-emission scanning electron microscope (FE-SEM) images. The X-ray diffraction (XRD) and the X-ray photoelectron spectroscopy (XPS) were recorded on a M18XHF SRA (MAC Science Co.) and AXIS-HIs (KRATOS), respectively. The FTIR spectrum was recorded on a Bomem MB 100 spectroscope (Quebec, Canada) in the absorption mode. The measurement of the electrical conductivity was carried out with a source-meter at ambient temperature by a four-probe method. The Raman spectrum and TGA analyses were recorded on a T64000 (HORIABA Jobin Yvon) and Pyris6 (Perkin-Elmer), repectively.

Electrical Measurement of Sensitivities in Hybrid CNF Sensors. The resistance changes of hybrid CNFs were monitored with a source-meter connected to a computer. The hybrid CNF sensors were placed in a 350 mL vacuum chamber with a vapor inlet/outlet at ~100 Torr, and then various DMMP gas concentrations (0.1−1000 ppb) were injected into the chamber by the mass flow controller (MFC, KNH Instruments). The resistance values were recorded in real time at a constant applied current of 10^{-7} A. After hybrid CNFs interacted with DMMP gas concentrations (0.1−1000 ppb) for several minutes, each vapor was replaced by compressed air to remove the DMMP molecules attached on the backbone of the nanomaterials. This process was performed repeatedly several times. Vapor/air was supplied at various flow rates of 2−8 slm and 1−5 sccm controlled by MFC. The real-time resistance was monitored at a constant applied current of 10^{-7} A (defined as $\Delta R/R_0 = (R - R_0)/R_0$, where R and R_0 are the real-time resistance and the initial resistance, respectively).

Acknowledgment. This research was supported by the WCU (World Class University) program through the National Research Foundation of Korea funded by the Ministry of Education, Science and Technology (R31-10013) and the National Research Foundation of Korea (NRF) grant funded by the Korea government (MEST) (No. 2011-0017125).

Supporting Information Available: The contents of the Supporting Information include the following: (1) optical microscope image of phase-separated mixed solution; (2) schematic illustration of fabrication hybrid nanofiber with ZnO/SnO_2 nanonodules; (3) Raman spectrum of hybrid NFs and hybrid CNFs; (4) FE-SEM images of electrospun NFs made from PAN and PAN/PVP solutions; (5) FE-SEM images of hybrid CNFs made from PAN and PAN/PVP solutions; (6) TGA analyses of metal oxide decoration amount; (7) FE-SEM images and $I-V$ graph of CNF3 on the IDA made by drop-casting and spin-coating methods; (8) sensitivity curve of CNF3 at constant DMMP concentration as a function of metal oxide concentration; (9) sensing performance of CNF3 with changing metal oxide concentration. This material is available free of charge *via* the Internet at http://pubs.acs.org.

REFERENCES AND NOTES

1. Baughman, R. H.; Zakhidov, A. A.; De Heer, W. A. Carbon Nanotubes—The Route toward Applications. *Science* **2002**, *297*, 787–792.
2. Fan, Z. J.; Yan, J.; Wei, T.; Ning, G. Q.; Zhi, L. J.; Liu, J. C.; Cao, D. X.; Wang, G. L.; Wei, F. Nanographene-Constructed Carbon Nanofibers Grown on Graphene Sheets by Chemical Vapor Deposition: High-Performance Anode Materials for Lithium Ion Batteries. *ACS Nano* **2011**, *5*, 2787–2794.
3. Chiang, W. H.; Sankaran, R. M. Linking Catalyst Composition to Chirality Distributions of As-Grown Single-Walled Carbon Nanotubes by Tuning Ni_xFe_{1-x} Nanoparticles. *Nat. Mater.* **2009**, *8*, 882–886.
4. Lee, K. J.; Shiratori, N.; Lee, G. H.; Miyawaki, J.; Mochida, I.; Yoon, S. H.; Jang, J. Activated Carbon Nanofiber Produced from Electrospun Polyacrylonitrile Nanofiber as a Highly Efficient Formaldehyde Adsorbent. *Carbon* **2010**, *48*, 4248–4255.

5. Xie, X.; Hu, L.; Pasta, M.; Wells, G. F.; Kong, D.; Criddle, C. S.; Cui, Y. Three-Dimensional Carbon Nanotube-Textile Anode for High-Performance Microbial Fuel Cells. *Nano Lett.* **2011**, *11*, 291–296.
6. Xu, Y. J.; Zhuang, Y.; Fu, X. New Insight for Enhanced Photocatalytic Activity of TiO_2 by Doping Carbon Nanotubes: A Case Study on Degradation of Benzene and Methyl Orange. *J. Phys. Chem. C* **2010**, *114*, 2669–2676.
7. Kauffman, D. R.; Star, A. Carbon Nantube Gas and Vapor Sensors. *Angew. Chem., Int. Ed.* **2008**, *47*, 6550–6570.
8. Niu, H.; Zhang, J.; Xie, Z.; Wang, X.; Lin, T. Preparation, Structure and Supercapacitance of Bonded Carbon Nanofiber Electrode Materials. *Carbon* **2011**, *49*, 2380–2388.
9. Gong, K.; Chakrabarti, S.; Dai, L. Electrochemistry at Carbon Nanotube Electrodes: Is the Nanotube Tip More Active Than the Sidewall? *Angew Chem., Int. Ed.* **2008**, *47*, 5446–5450.
10. Yu, Y.; Gu, L.; Zhu, C.; Van Aken, P. A.; Maier, J. Tin Nanoparticles Encapsulated in Porous Multichannel Carbon Microtubes: Preparation by Single-Nozzle Electrospinning and Application as Anode Material for High-Performance Li-Based Batteries. *J. Am. Chem. Soc.* **2009**, *131*, 15984–15985.
11. Palmeri, M. J.; Putz, K. W.; Brinson, L. C. Sacrificial Bonds in Stacked-Cup Carbon Nanofibers: Biomimetic Toughening Mechanisms for Composite Systems. *ACS Nano* **2010**, *4*, 4256–4264.
12. Kim, C.; Jeong, Y. I.; Ngoc, B. T. N.; Yang, K. S.; Kojima, M.; Kim, Y. A.; Endo, M.; Lee, J. W. Synthesis and Characterization of Porous Carbon Nanofibers with Hollow Cores through the Thermal Treatment of Electrospun Copolymeric Nanofiber Webs. *Small* **2007**, *3*, 91–95.
13. Han, J. H.; Paulus, G. L. C.; Maruyama, R.; Heller, D. A.; Kim, W. J.; Barone, P. W.; Lee, C. Y.; Choi, J. H.; Ham, M. H.; Song, C.; *et al.* Exciton Antennas and Concentrators from Core–Shell and Corrugated Carbon Nanotube Filaments of Homogeneous Composition. *Nat. Mater.* **2010**, *9*, 833–839.
14. Lin, Z.; Ji, L.; Woodroof, M. D.; Yao, Y.; Krause, W.; Zhang, X. Synthesis and Electrocatalysis of Carbon Nanofiber-Supported Platinum by 1-AP Functionalization and Polyol Processing Technique. *J. Phys. Chem. C* **2010**, *114*, 3791–3797.
15. Kvande, I.; Zhu, J.; Zhao, T. J.; Hammer, N.; Rønning, M.; Raaen, S.; Walmsley, J. C.; Chen, D. Importance of Oxygen-Free Edge and Defect Sites for the Immobilization of Colloidal Pt Oxide Particles with Implications for the Preparation of CNF-Supported Catalysts. *J. Phys. Chem. C* **2010**, *114*, 1752–1762.
16. Hiralal, P.; Imaizumi, S.; Unalan, H. E.; Matsumoto, H.; Minagawa, M.; Rouvala, M.; Tanioka, A.; Amaratunga, G. A. J. Nanomaterial-Enhanced All-Solid Flexible Zinc-Carbon Batteries. *ACS Nano* **2010**, *4*, 2730–2734.
17. Celebi, S.; Nijhuis, T. A.; Van Der Schaaf, J.; De Bruijn, F. A.; Schouten, J. C. Carbon Nanofiber Growth on Carbon Paper for Proton Exchange Membrane Fuel Cells. *Carbon* **2011**, *49*, 501–507.
18. Choi, S. H.; Ankonina, G.; Youn, D. Y.; Oh, S. G.; Hong, J. M.; Rothschild, A.; Kim, I. D. Hollow ZnO Nanofibers Fabricated Using Electrospun Polymer Templates and Their Electronic Transport Properties. *ACS Nano* **2009**, *3*, 2623–2631.
19. Wang, B.; Zhu, L. F.; Yang, Y. H.; Xu, N. S.; Yang, G. W. Fabrication of a SnO_2 Nanowire Gas Sensor and Sensor Performance for Hydrogen. *J. Phys. Chem. C* **2008**, *112*, 6643–6647.
20. Landau, O.; Rothschild, A.; Zussman, E. Processing-Microstructure-Properties Correlation of Ultrasensitive Gas Sensors Produced by Electrospinning. *Chem. Mater.* **2009**, *21*, 9–11.
21. Zhang, Z.; Li, X.; Wang, C.; Wei, L.; Liu, Y.; Shao, C. ZnO Hollow Nanofibers: Fabrication from Facile Single Capillary Electrospinning and Applications in Gas Sensors. *J. Phys. Chem. C* **2009**, *113*, 19397–19403.
22. Jang, J. Conducting Polymer Nanomaterials and Their Applications. *Adv. Polym. Sci.* **2006**, *199*, 189–259.
23. Hatchett, D. W.; Josowicz, M. Composites of Intrinsically Conducting Polymers as Sensing Nanomaterials. *Chem. Rev.* **2008**, *108*, 746–769.
24. Yoon, H.; Jang, J. Conducting-Polymer Nanomaterials for High-Performance Sensor Applications: Issues and Challenges. *Adv. Funct. Mater.* **2009**, *19*, 1567–1576.
25. Gong, J.; Li, Y.; Hu, Z.; Zhou, Z.; Deng, Y. Ultrasensitive NH_3 Gas Sensor from Polyaniline Nanograin Enchased TiO_2 Fibers. *J. Phys. Chem. C* **2010**, *114*, 9970–9974.
26. Lee, D. H.; Lee, J. A.; Lee, W. J.; Choi, D. S.; Lee, W. J.; Kim, S. O. Facile Fabrication and Field Emission of Metal-Particle-Decorated Vertical N-Doped Carbon Nanotube/Graphene Hybrid Films. *J. Phys. Chem. C* **2010**, *114*, 21184–21189.
27. Lee, W. J.; Lee, D. H.; Han, T. H.; Lee, S. H.; Moon, H. S.; Lee, J. A.; Kim, S. O. Biomimetic Mineralization of Vertical N-Doped Carbon Nanotubes. *Chem. Commun.* **2011**, *47*, 535–537.
28. Lee, D. H; Lee, W. J.; Kim, S. O. Highly Efficient Vertical Growth of Wall-Number-Selected, N-Doped Carbon Nanotube Arrays. *Nano Lett.* **2009**, *9*, 1427–1432.
29. Yang, Z.; Du, G.; Guo, Z.; Yu, X.; Li, S.; Chen, Z.; Zhang, P.; Liu, H. Plum-Branch-like Carbon Nanofibers Decorated with SnO_2 Nanocrystals. *Nanoscale* **2010**, *2*, 1011–1017.
30. Zhang, H. X.; Feng, C.; Zhai, Y. C.; Jiang, K. L.; Li, Q. Q.; Fan, S. S. Cross-Stacked Carbon Nanotube Sheets Uniformly Loaded with SnO_2 Nanoparticles: A Novel Binder-Free and High-Capacity Anode Material for Lithium-Ion Batteries. *Adv. Mater.* **2009**, *21*, 2299–2304.
31. Bazilevsky, A. V.; Yarin, A. L.; Megaridis, C. M. Co-electrospinning of Core–Shell Fibers Using a Single-Nozzle Technique. *Langmuir* **2007**, *23*, 2311–2314.
32. Xu, X.; Zhuang, X.; Chen, X.; Wang, X.; Yang, L.; Jing, X. Preparation of Core-Sheath Composite Nanofibers by Emulsion Electrospinning. *Macromol. Rapid Commun.* **2006**, *27*, 1637–1642.
33. Zussman, E.; Yarin, A. L.; Bazilevsky, A. V.; Avrahami, R.; Feldman, M. Electrospun Polyacrylonitrile/Poly(methyl methacrylate)-Derived Turbostratic Carbon Micro-/Nanotubes. *Adv. Mater.* **2006**, *18*, 348–353.
34. McCann, J. T.; Marquez, M.; Xia, Y. Melt Coaxial Electrospinning: A Versatile Method for the Encapsulation of Solid Materials and Fabrication of Phase Change Nanofibers. *Nano Lett.* **2006**, *6*, 2868–2872.
35. Lagerwall, J. P. F.; McCann, J. T.; Formo, E.; Scalia, G.; Xia, Y. Coaxial Electrospinning of Microfibres with Liquid Crystal in the Core. *Chem. Commun.* **2008**, 5420–5422.
36. Dale, T. J.; Rebek, J., Jr. Hydroxy Oximes as Organophosphorus Nerve Agent Sensors. *Angew. Chem., Int. Ed.* **2009**, *48*, 7850–7852.
37. Ji, X.; Zheng, J.; Xu, J.; Rastogi, V. K.; Cheng, T. C.; DeFrank, J. J.; Leblanc, R. M. (CdSe)ZnS Quantum Dots and Organophosphorus Hydrolase Bioconjugate as Biosensors for Detection of Paraoxon. *J. Phys. Chem. B* **2005**, *109*, 3793–3799.
38. Hartmann-Thompson, C.; Hu, J.; Kaganove, S. N.; Keinath, S. E.; Keeley, D. L.; Dvornic, P. R. Hydrogen-Bond Acidic Hyperbranched Polymers for Surface Acoustic Wave (SAW) Sensors. *Chem. Mater.* **2004**, *16*, 5357–5364.
39. Wang, F.; Gu, H.; Swager, T. M. Carbon Nanotube/Polythiophene Chemiresistive Sensors for Chemical Warfare Agents. *J. Am. Chem. Soc.* **2008**, *130*, 5392–5393.
40. Snow, E. S.; Perkins, F. K.; Houser, E. J.; Badescu, S. C.; Reinecke, T. L. Chemical Detection with a Single-Walled Carbon Nanotube Capacitor. *Science* **2005**, *307*, 1942–1945.
41. Roberts, M. E.; Lemieux, M. C.; Bao, Z. Sorted and Aligned Single-Walled Carbon Nanotube Networks for Transistor-Based Aqueous Chemical Sensors. *ACS Nano* **2009**, *3*, 3287–3293.
42. Zhang, Z.; Shao, C.; Li, X.; Zhang, L.; Xue, H.; Wang, C.; Liu, Y. Electrospun Nanofibers of ZnO-SnO_2 Heterojunction with High Photocatalytic Activity. *J. Phys. Chem. C* **2010**, *114*, 7920–7925.
43. Kwon, O. S.; Hong, J. Y.; Park, S. J.; Jang, Y.; Jang, J. Resistive Gas Sensors Based on Precisely Size-Controlled Polypyrrole Nanoparticles: Effects of Particle Size and Deposition Method. *J. Phys. Chem. C* **2010**, *114*, 18874–18879.
44. Lee, C. Y.; Sharma, R.; Radadia, A. D.; Masel, R. I.; Strano, M. S. On-Chip Micro Gas Chromatograph Enabled by a Noncovalently

Functionalized Single-Walled Carbon Nanotube Sensor Array. *Angew. Chem., Int. Ed.* **2008**, *47*, 5018–5021.
45. Lee, S. C.; Choi, H. Y.; Lee, S. J.; Lee, W. S.; Huh, J. S.; Lee, D. D.; Kim, J. C. The Development of SnO_2-Based Recoverable Gas Sensors for the Detection of DMMP. *Sens. Actuators, B* **2009**, *137*, 239–245.